Experiments in Fluids (2025) 66:112
https://doi.org/10.1007/s00348-025-04043-8

RESEARCH ARTICLE

Application of BOS velocimetry to full-scale helicopter flight tests

Johannes N. Braukmann[1] · C. Christian Wolf[1] · Anthony D. Gardner[1]

Received: 10 February 2025 / Revised: 22 April 2025 / Accepted: 23 April 2025

Abstract

Time-resolved background-oriented schlieren (BOS) data are used to calculate the two-dimensional velocity field in the wake of free-flying full-scale helicopters in ground effect. The calculation is performed based on the density gradient pattern of the helicopter engine exhaust gas passing the BOS field of view. A classical BOS evaluation allows the visualization of density gradients such as vortices and the exhaust plume. The result is the BOS displacement field. Applying the two-dimensional divergence to these data results in a pattern that is constant in shape across multiple BOS images, but convects downstream with the outwash velocity of the helicopter. Quantitative two-dimensional velocity fields are calculated using the divergence of the BOS shift as input to a second, time-resolved evaluation. Choosing an appropriate strategy for preparing and evaluating the data is critical to a reliable velocity estimation. Another important aspect is to distinguish between reliable velocity data and erroneous results in areas of reduced signal intensity due to a lack of thermal structures. The velocity data obtained are compared with an analytical outwash model and constant temperature anemometry data acquired simultaneously with the BOS images. The data show good quantitative agreement in areas of sufficient thermal structures within the field of view. This demonstrates the feasibility of BOS velocimetry to investigate large flow fields in full-scale helicopter flight tests.

List of symbols

f	Lens focal length, m
h	Normalized rotor hub height, y_{hub}/R
M_{obj}	Magnification factor with respect to object plane
R	Rotor radius, m
t	Time, s
V	Absolute velocity, m/s
V_{h}	Hover–induced velocity, m/s
V_x	Velocity in x-direction, m/s
V_y	Velocity in y-direction, m/s
x, y, z	Cartesian coordinates, m
z_A	Distance between lens and object, m
z_B	Distance between lens and background, m
z_i	Distance between lens and camera sensor, m
Δ	Difference between two values
BOS	Background–oriented schlieren
CTA	Constant temperature anemometry
DLR	German Aerospace Center
FOV	Field of view
IGE	In ground effect
PIV	Particle image velocimetry
SIV	Schlieren image velocimetry
SPR	Stereo pattern recognition

1 Introduction

The wake of a helicopter is a highly complex and three-dimensional flow field. Strong spatial gradients, vortices and high temporal fluctuations dominate the flow. During operation in ground proximity the helicopter wake is deflected outward, and the complexity of the flow increases. As a result, the numerical prediction is challenging and demands validation data. Typical techniques used to measure a helicopter rotor wake in ground effect (IGE) are point-wise measurements, such as sonic anemometers (Silva and Riser 2011), pressure probes (Tanner et al. 2015), laser Doppler velocimetry and lidar sensors (Sugiura et al. 2017) or hot-wires and hot-film sensors (Saijo et al. 2003). Capturing the entire azimuth-dependent and instationary outwash topology of a helicopter with these techniques requires a high effort either in measurement

✉ Johannes N. Braukmann
Johannes.Braukmann@DLR.de

C. Christian Wolf
Christian.Wolf@DLR.de

Anthony D. Gardner
Tony.Gardner@DLR.de

[1] Institute of Aerodynamics and Flow Technology, German Aerospace Center (DLR), Bunsenstr. 10, 37073 Göttingen, Germany

Published online: 25 May 2025

time or in setting up a large array of sensors. Planar measurements, such as particle image velocimetry (PIV) also require a lot of effort and are limited in size due to the light intensity required. In addition, safety concerns when working with high power lasers limit the options.

Over the last few years, multirotor aircraft are gaining popularity in addition to common helicopters. The down- and outwash of these aircraft are far more complex and yet far less studied (Brown 2023). As a result, there is a high demand for suitable and easy to use measurement techniques to characterize the outwash topology of modern aircraft.

In the last decades, the background-oriented schlieren (BOS) technique has gained interest in the helicopter community. Based on a relatively simple test setup, density gradients in the flow can be visualized and under certain conditions even quantified. The technique requires a sufficiently illuminated background with a high-contrast pattern and a camera focused on that background. Due to the refraction of light by density gradients along the line of sight, flow phenomena such as blade tip vortices and even the blades' shear layers can be visualized. Due to the simple setup, large fields of view (FOV) can be realized, which is a major advantage over classical schlieren setups.

Classical schlieren images of turbulent flows allow for the quantitative evaluation of the convection velocity of the turbulent structures. Jonassen et al. (2006) demonstrated the feasibility of this technique to measure the velocity field of an axisymmetric sonic helium jet in air and a two-dimensional turbulent boundary layer at Mach 3 using commercial PIV equipment combined with schlieren optics. They showed, that turbulent eddies can be utilized as a replacement for PIV seeding particles.

Mittelstaedt et al. (2010) used a background focused approach, comparable to a BOS setup, to measure the velocity of a diffuse hydrothermal flow. Following laboratory tests on a laminar, axisymmetric plume in fluids with both constant and temperature dependent viscosity they applied the technique to video sequences of a diffuse flow and estimated the velocity of the plumes in good agreement with previous reference measurements.

A comparison between schlieren, shadowgraph, and focusing schlieren images as basis for velocity measurements was carried out by Hargather et al. (2011). Here, naturally occurring refractive turbulent eddies in a flow were used as virtual seed particles. They conclude that schlieren image velocimetry (SIV) is a potentially useful seedless velocimetry technique that is capable of performing velocimetry measurements using naturally occurring turbulent eddies within a flow as a replacement for classical PIV particles.

Biswas and Qiao (2017) applied SIV to a turbulent helium jet and compared the results to PIV measurements. Following the authors, the calculated velocities showed excellent agreement with the PIV measurements. An impression of the recorded images as well as the obtained velocity data is shown in Fig. 1. Besides the PIV results on the left, also schlieren images with different knife-edge orientations as well as a shadowgraph example can be seen.

More recently, Settles and Liberzon (2022) stated that seedless velocimetry is gaining interest in many industrial and research applications. They compared traditional,

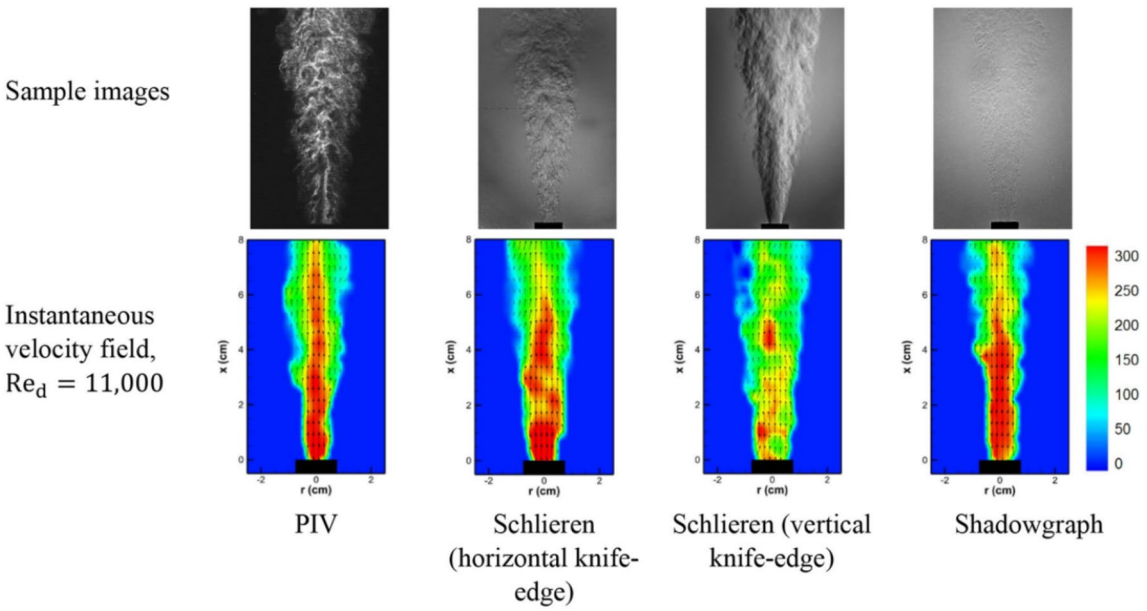

Fig. 1 Sample images and instantaneous velocity fields of a turbulent helium jet from PIV, schlieren, and shadowgraph measurements by Biswas and Qiao (2017)

mirror-type knife-edge schlieren optics and BOS data as input for a correlation-based quantitative evaluation of the velocity field. Both techniques were applied to subsonic, round, and turbulent helium jets in air at different Reynolds numbers.

In summary, it has been shown that schlieren images, shadowgraph images, and also BOS data can be used as input for a quantitative estimation of the flow velocity, if turbulent structures or other density fluctuations are present and can be used as seedless tracer patterns. The objective of this paper is to demonstrate the feasibility of this BOS velocimetry to full-scale in-flight tests of helicopters IGE. As a first step the outwash topology will be analyzed qualitatively and in a second step the gained quantitative velocity data will be compared to constant temperature anemometry (CTA) data and to an analytic outwash model.

2 Experimental setup

The BOS data were obtained during two flight campaigns featuring a CH-53G and a Bo105 helicopter. Both flight tests were conducted at the Braunschweig regional airport (EDVE). The main parameters of the helicopters and the test cases used in this paper can be found in Table 1.

Hover cases at a hub height above ground of $h = 0.61$ in case of the CH-53G and $h = 0.87$ in case of the Bo105 are investigated. An overview of the test setup is shown in Fig. 2 with the hovering CH-53G helicopter next to the CTA array and the BOS camera setup in the background. Details of both campaigns can be found in Braukmann et al. (2023) and Wolf et al. (2022).

For the BOS recordings a Phantom VEO 640 high-speed camera was used at a recording frequency of 420Hz. Density gradients between the camera and the background lead to a refraction of light rays originating from the background and, thus, to an apparent displacement of a background pattern on the camera's sensor (Raffel 2015). The camera was focused on a hangar wall covered with retro-reflective foil. The foil featured a high-contrast dot pattern. The sizes of the dots were chosen to result in a dot image size of approximately 3px on the camera sensor in both setups. Four LED spots were located close to each BOS camera to homogeneously illuminate the background. For each test case, either 6000 or 9000 images were recorded during the CH-53G and the Bo105 campaign, respectively.

Figure 3 shows a sample BOS result from the Bo105 measurement. At the top, remnants of a blade tip vortex can be seen. In the lower left part, the exhaust gas from the engine is visible. The strong thermal gradients cause strong density gradients which can be seen in the BOS results.

The grayscale image in Fig. 3 shows the two-dimensional divergence of the BOS displacement field which corresponds to

$$\frac{\partial^2 \rho}{\partial x^2} + \frac{\partial^2 \rho}{\partial y^2}. \tag{1}$$

These data are often used to detect the blade tip vortices and to reconstruct the shape of the rotor wake. In the current campaign the vortices were found to fall below the detection limit of the BOS system quite rapidly and, thus, are not seen in the chosen FOV for most of the images.

Table 1 Parameters of the two helicopters and the respective test cases

Parameter	CH-53G	Bo105
R (m)	11.00	4.91
No of blades	6	4
Gross mass (kg)	13367	2194
V_h (m/s)	11.87	11.02
h	0.61	0.87

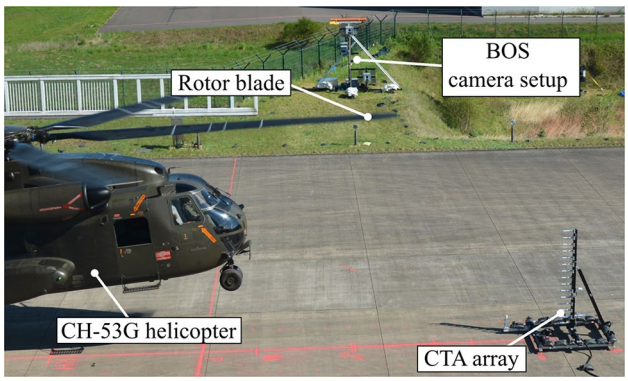

Fig. 2 Overview of the test setup with the CH-53G helicopter in hover

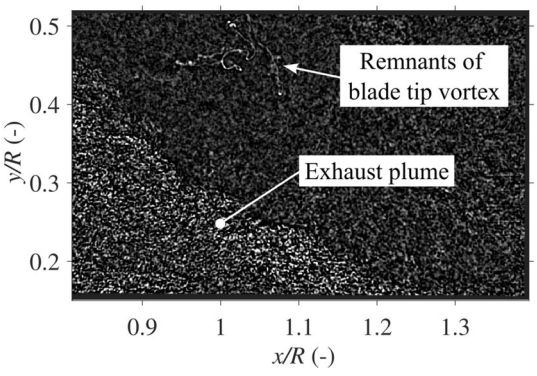

Fig. 3 Sample image showing the two-dimensional divergence of the BOS displacement in the wake of the Bo105

The divergence operator emphasizes the pattern caused by the exhaust plume in the turbulent wake of the main rotor. The resulting pattern is stable and convects with the outwash velocity. This phenomenon can be seen with the naked eye by comparing successive vector fields of the 420Hz recording. The data are used in a second correlation to quantify the convection velocity as described by Settles and Liberzon (2022) and Mittelstaedt et al. (2010).

A sketch of the test setups for both CH-53G and Bo105 is shown in Fig. 4. In both cases a horizontal BOS FOV is chosen to capture the outwash velocities in ground proximity and to enable a quantitative comparison with the velocity profile measured by the CTA array. The FOVs have a size of 5.45m×3.41m ($0.50R \times 0.31R$) in the case of the CH-53G and 2.87m×1.79m ($0.58R \times 0.36R$) in the Bo105 case. During the CH-53G experiments the FOV was positioned even closer to the ground, covering the height of the entire CTA array. The sketches feature a line as visual guidance at the approximate position of the slipstream boundary with respect to the test geometry.

Vertical CTA arrays were utilized in both campaigns to capture the velocity profiles in ground proximity (see Fig. 5). The arrays consisted of 15 "TSI 1201" fiber-film probes. Each probe is made of a platinum film sensor wrapped around a quartz cylinder of 50.8 μm in diameter and 1.27mm in length. Compared to hot-wire probes the fiber-film sensors are more robust regarding particle impacts, but feature a lower frequency limit of approximately 10kHz. The data are calibrated based on the temperature-linearized King's law (Bruun 1995) and a calibration measurement in a wind tunnel of DLR Göttingen. During the downwash measurement the ambient temperature was measured by Pt100 sensors positioned within the CTA array. The position of the arrays with respect to the helicopters and the BOS FOVs can be seen in Fig. 4. Since the data of the CTA arrays and the BOS images are taken time-synchronized, a quantitative comparison can be made. Details of the CTA measurements can be found in Braukmann et al. (2023) and Wolf et al. (2022).

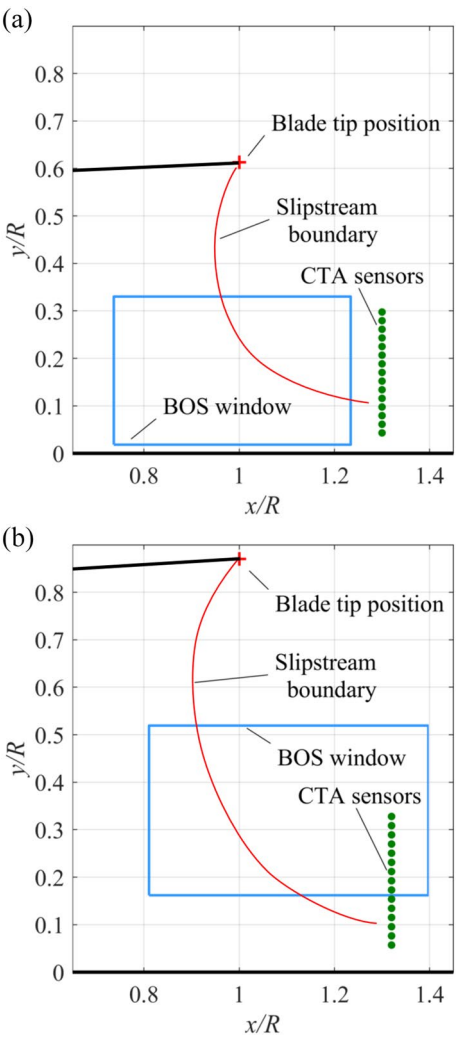

Fig. 4 Sketches of the measurement setups. **a** CH-53G campaign, **b** Bo105 campaign. Adapted from Wolf et al. (2022)

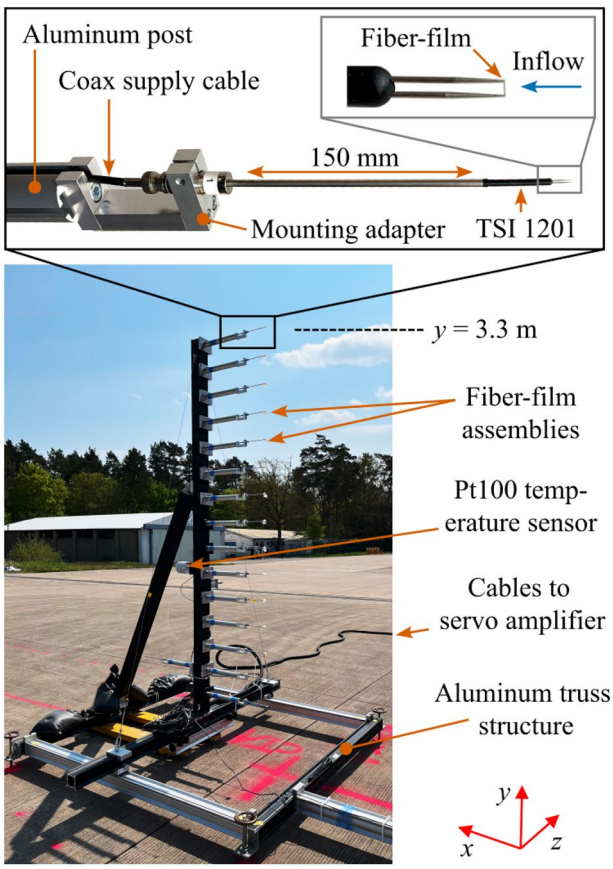

Fig. 5 Details of the fiber-film CTA sensor rake. From Braukmann et al. (2023)

The hot exhaust gas used for the BOS velocimetry evaluation is passing the CTA array during the measurements. Therefore, an influence on the CTA measurement cannot be avoided. To estimate the influence on the velocity measurement, the Pt100 temperature sensors close to the CTA array can be used. The measured temperature during the test cases used in this paper stay within a 2K range which is considered negligible compared to the fiber-film temperature of 560K.

3 Data evaluation

The BOS images are evaluated using a standard approach: A reference image without the influence of the helicopter is correlated with each measurement image using interrogation windows with decreasing sizes down to 12pixels in diameter with an overlap of 75%. The velocity components for each window are calculated based on the local shift Δd and the time between two subsequent images Δt using $V_x = \Delta x/\Delta t$ and $V_y = \Delta y/\Delta t$, respectively. The result is a vector field with a spacing of 6.4mm in the case of the CH-53G data and 3.4mm in the case of the Bo105 data. The correlations are performed using LaVision DaVis 11.0.

Samples of intensity patterns can be seen in Fig. 6. The cutouts of 51×51pixels of a reference and a measurement image used for the first standard BOS correlation are shown in Fig. 6a) and b), respectively. The dots printed on the background foil form a high-contrast dot pattern which can be used for the correlation-based displacement detection. The dots in the measurement image (Fig. 6b)) appear blurry compared to the reference image due to the influence of the hot exhaust gas from the engines. The strong gradients cause an unsharp imaging of the background pattern in addition to the expected displacement. Nonetheless, the correlation of both signals leads to a reliable displacement detection due to the robustness of the correlation approach. The evaluation approach is optimized for structure sizes of 3px. Smaller structures can introduce peak locking, whereas significantly larger structures limit the spatial resolution.

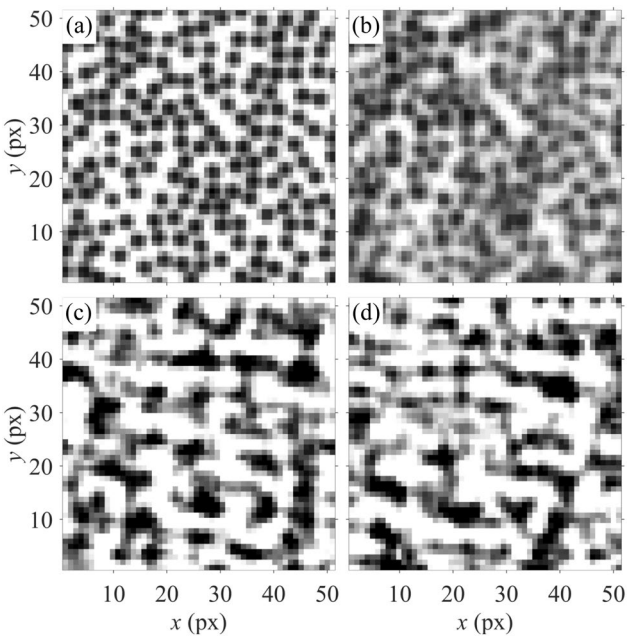

Fig. 6 Sample intensity cutouts from **a** the reference image of the first correlation, **b** a measurement image of the first correlation, **c** an image used in the second correlation, and **d** the succeeding image to **c**

Figure 6c and d shows the cutouts of two subsequent divergence fields. Again, a high-contrast pattern can be seen. This two-dimensional divergence of the BOS displacement field is extracted and used as input for a second correlation. The pattern moves with the convection velocity of the exhaust plume in the rotor wake. This feature enables a detection of the outwash velocities in areas of the engine exhaust. The quality and temporal stability of the correlation input is reduced in comparison with the input data of the first correlation, but still allows for a reliable velocity estimation.

The signal features positive and negative values since it is the two-dimensional divergence of the BOS displacement field according to Eq. (1). To optimize the data as input for the second correlation the minimum of each pixel over three subsequent images is subtracted in each image to remove steady structures in the images. To avoid artifacts during this step, first the absolute value of each pixel is calculated, removing negative values, but keeping the characteristics of the pattern. The signal preprocessing leads to an increase of the image contrast.

To account for the reduced data quality an ensemble-averaging (sliding sum of correlation) approach was used during the second correlation. This technique enables a reduction of noise and a reduction of the correlation windows' size using the results of several (subsequent) image pairs assuming a stationary flow over the chosen filter length (Meinhart et al. 2000). For the current evaluation a filter length of ± 25 image pairs around each result was used ($\approx 1/8$s). The final correlation windows had a diameter of 8pixels and an overlap of 75%. These settings lead to a final grid spacing of 12.8mm for the data of the CH-53G downwash and 6.8mm in case of the Bo105. The maximum pixel displacement was 15pixels in the case of the CH-53G and 20pixels in the case of the Bo105.

A spatial calibration of the camera setup is necessary to quantitatively interpret the velocity data. The spatial displacement of the thermal pattern and the known time between two subsequent images are used to calculate the velocity of the structures. The BOS setups were calibrated in the x-y-plane using a reference plate featuring a dot pattern with a spacing of 0.1m. The resulting two-dimensional calibration of the camera perspective is only correct in the

selected reference plane. A detection of structures in front of or behind this plane leads to errors in the velocity calculation. The geometric parameters of a BOS setup assuming a pinhole model are illustrated in Fig. 7. The distance between camera and object plane (z_A) and between camera and background (z_B) is given by the overall geometry of the BOS setup. With the focal length f the distance z_i can be calculated by the lens equation assuming the camera is focused on the background plane:

$$\frac{1}{f} = \frac{1}{z_i} + \frac{1}{z_B} \Leftrightarrow z_i = \frac{1}{\frac{1}{f} - \frac{1}{z_B}}.$$

Based on these parameters, the magnification factor of an object in the calibrated object plane is given by $M_{\text{obj}} = z_i/z_A$. A deviation of the actual object plane from the calibrated object plane leads to an error in the magnification factor, which is proportional to the error in the velocity calculation. The relative error in the magnification factor as function of a deviation from the calibrated object plane is given in Fig. 8.

It can be seen, that a deviation from the calibrated object plane in the order of the rotor radii leads to errors of ±25% for the CH-53G and 20% for the Bo105. This influence has to be kept in mind during a quantitative interpretation of the velocity distributions. Due to the ambient wind conditions in both campaigns the exhaust plume was convected from the engine outlets close to the rotor center in the forward direction through the FOV of the BOS setup. Based on a careful observation of the flow conditions it is assumed that the tracer gas is found within the rotor diameter when passing the BOS FOV and the resulting error thus is below 25% or 20%, respectively.

4 Results

The exhaust plume covers different areas of the BOS FOV throughout the measurement time. A typical plume distribution in case of the CH-53G can be seen in Fig. 9a). The

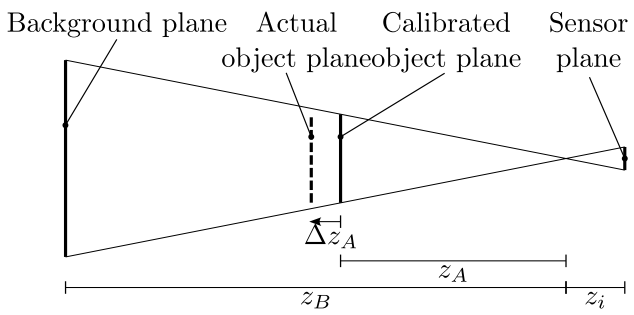

Fig. 7 Distances of the camera setup according to the pinhole model

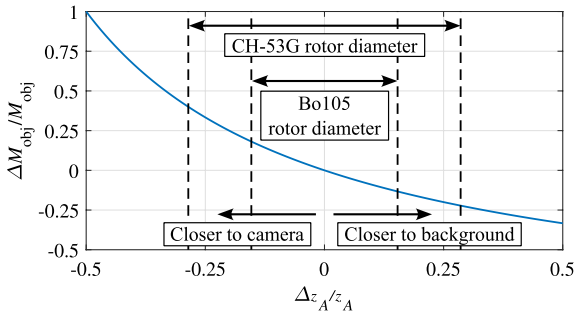

Fig. 8 Influence of an offset between the calibrated object plane and the location of the exhaust plume on the velocity estimation

intensity distribution is a result of the first correlation and shows the maximum two-dimensional divergence of each pixel over ±25 images around a sample image. The image span corresponds to the number of images used for the sliding sum of correlation used for the velocity calculation. The bright area in the lover half of the image represents areas of sufficient seeding by thermal structures from the exhaust plume.

The upper half of the images does not contain the exhaust plume and therefore features a reduced intensity. The remaining contrast by thermal structures between the camera and the background still provides a pattern that leads to a correlation but with unreliable results. The results in areas

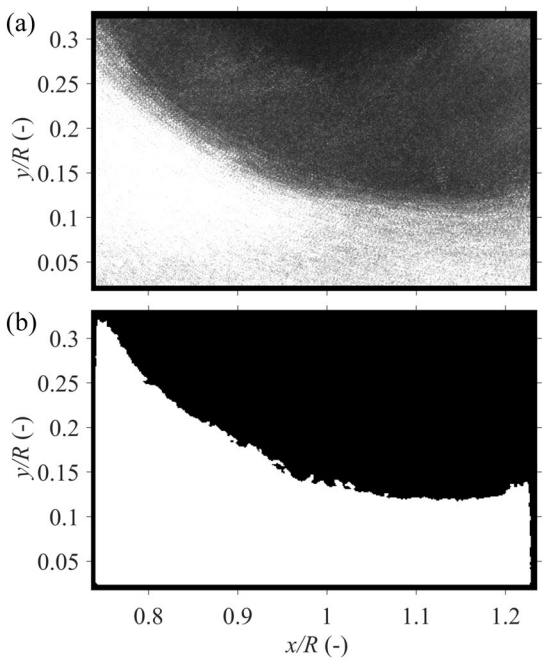

Fig. 9 Sample of a common outwash flow of the CH-53G. **a** Maximum intensity over ±25 images around sample image, indicating density gradients in white, **b** mask indicating area of reliable data in white derived from **a**

of low intensities are therefore detected and masked out. The corresponding mask is shown in Fig. 9b). The masking is performed using a two-dimensionally spatially smoothed intensity distribution and provides a reliable detection of those parts of the FOV containing exhaust plume.

Figure 10 shows the absolute in-plane velocity normalized by the hover induced velocity V_h with overlaid streamlines. The image corresponds to the intensity distribution and mask shown in Fig. 9. Areas without reliable thermal structures are depicted with a reduced opacity and the streamlines are limited to areas with reliable data. At the right side of the figure the 15 CTA sensor positions are indicated as black dots at $x/R = 1.32$. It can be seen that the area of reliable data only covers the lower third of the CTA array. It has to be noted, that the extent of the plume does not completely cover the rotor outwash. As a result, the border of the valid region does not indicate the slipstream boundary. Inside the area of valid data, the streamlines show a reasonable flow field.

In addition to the flow topology shown in Fig. 10, which dominates the 14.3s of BOS recording, several events of a large vortical upwash appear in the data. A sample intensity distribution of such an event is shown in Fig. 11a). The occurring structures do not originate from blade tip vortices, since the trajectories of the blade tip vortices documented in previous studies (Braukmann et al. 2023) do not match the location of the large-scale structures seen in the current BOS data. The structures occur randomly over time which suggests a relation to ambient wind conditions rather than a rotor harmonic cause.

The distinction between areas of sufficient intensity for a reliable correlation works well also for these events. Therefore, the BOS data are of great use to qualitatively analyze the instationary outwash topology and to determine the areas affected by the exhaust gas.

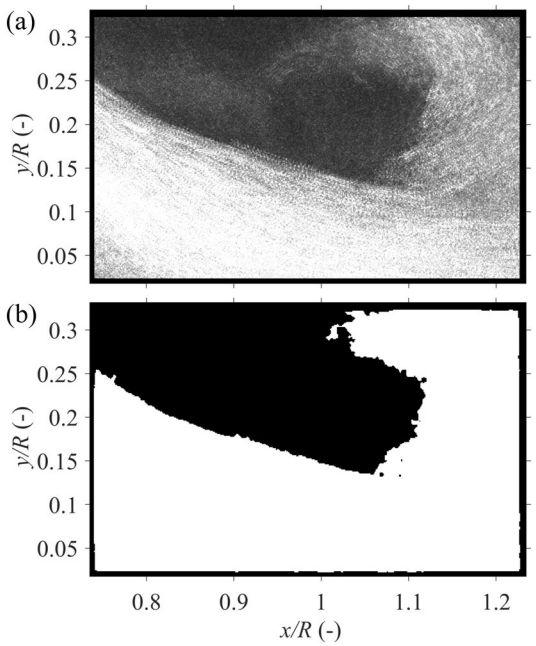

Fig. 11 Sample of a recirculating flow in the wake of the CH-53G. **a** Maximum intensity over ±25 images around sample image, indicating density gradients in white, **b** mask indicating area of reliable data in white derived from **a**

The calculated velocity field corresponding to the event of a vortical upwash is shown in Fig. 12. The streamlines in the lower part of the image follow the trend seen in Fig. 10. In the upper right corner of the image, the area of additional plume in Fig. 11a) the streamlines indicate a recirculation within the rotor outwash. The color-coded absolute velocity

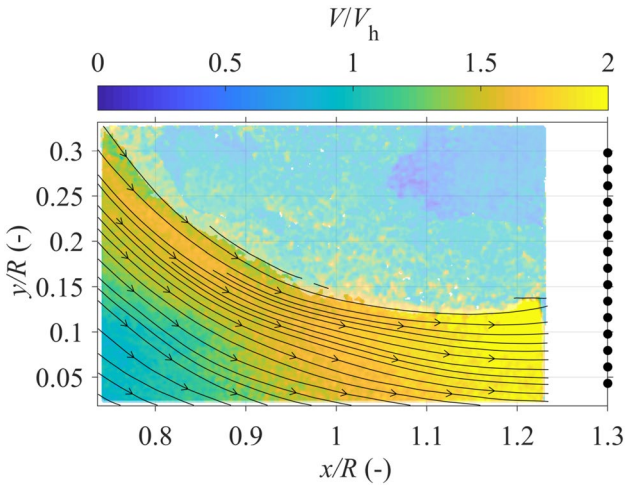

Fig. 10 Velocity distribution corresponding to the case shown in Fig. 9 with streamlines. Colors outside valid area desaturated

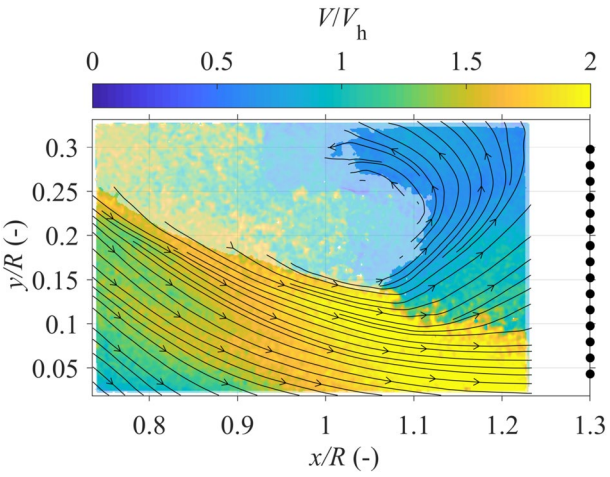

Fig. 12 Velocity distribution corresponding to the case shown in Fig. 11 with streamlines. Colors outside valid area desaturated

normalized by V_h shows a comparable magnitude in the region of the regular outwash. In the region of the upwash, the velocity magnitude is reduced and a rapid change between these two areas is apparent. The strong gradient between the two areas might be caused by two independent portions of exhaust gas at different locations between the camera and the background. In particular, the upward moving plume is assumed to be behind the horizontally moving plume convecting at a different velocity. In addition, the influence of the geometry of the BOS setup on the velocity estimation (discussed in Fig. 8) is adding to the differences in the detected convection velocities.

The detection of the exhaust plume also reliably works for the Bo105 data. Figure 13a) shows the maximum intensity of each pixel over ±25 images (0.12s) around a sample image indicating the area of the exhaust plume in white. A comparable outwash topology as shown in Fig. 9a) can be seen. At the right side of the image (above $x/R = 1.3$) no plume is found within the FOV. The reason for the lack of exhaust gas in this region is the higher position of the FOV above ground. The plume leaves the FOV at the bottom causing a lack of intensity suitable for correlation at higher x/R. Nonetheless, the detection of the exhaust plume works well also for the Bo105 data and the resulting mask can be seen in Fig. 13b).

The resulting velocity field of the Bo105 outwash is depicted in Fig. 14. The velocity estimation works as reliably, as for the CH-53G data, but at the height of the CTA sensors (black dots) no data are available in most of the recorded images. The area of the CTA array, which is located inside the BOS FOV in the Bo105 campaign had to be masked out to avoid an influence of the stationary sensors on the correlation-based velocity estimation.

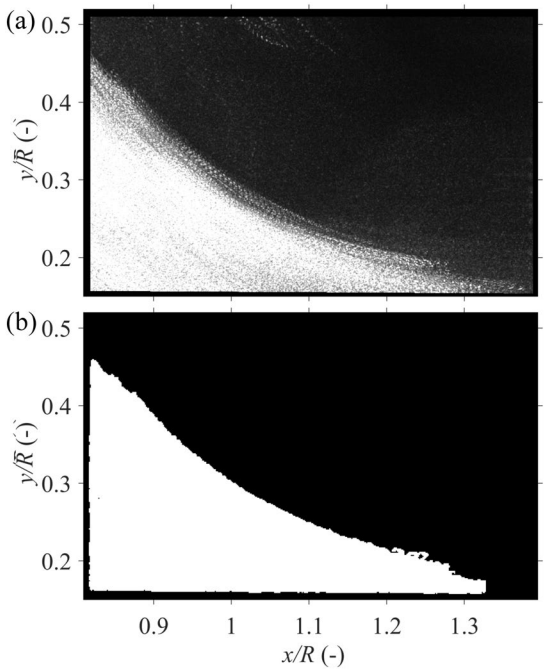

Fig. 13 Sample of a common outwash flow of the Bo105. **a** Maximum intensity over ±25 images around sample image, indicating density gradients in white, **b** mask indicating area of reliable data in white derived from **a**

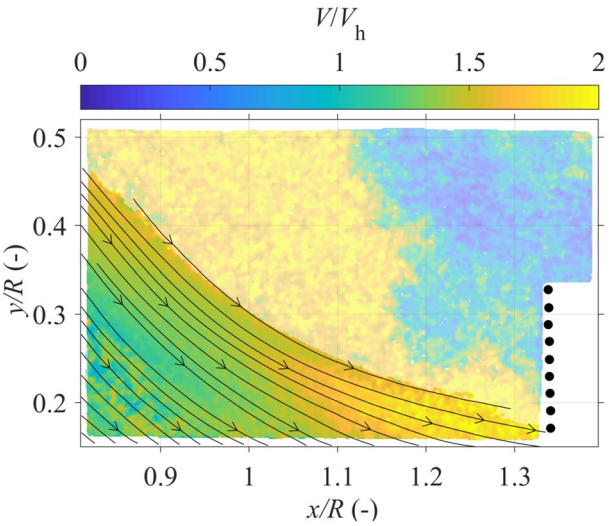

Fig. 14 Velocity distribution corresponding to the case shown in Fig. 13 with streamlines. Colors outside valid area desaturated

The percentage of valid data points over the height above ground is given in Fig. 15 for both data sets. The values indicate the amount of valid data among the images taken at a fixed position of $x/R = 1.20$ in the case of the CH-53G and $x/R = 1.31$ in the case of the Bo105. It can be seen that the Bo105 data do not provide enough reliable data near the CTA array at any height. Below $y/R = 0.1$ no data are obtained due to the limited FOV. Therefore, the velocity

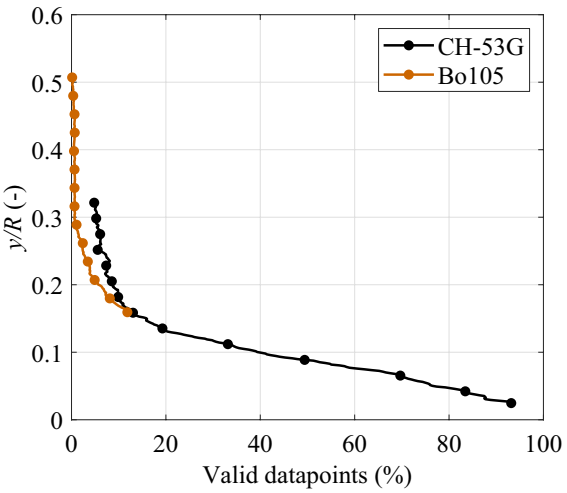

Fig. 15 Percentage of valid data over the normalized height above ground

data cannot be verified using the CTA velocity profiles. In the case of the CH-53G, the FOV was positioned closer to the ground plane, resulting in an increased number of images containing the exhaust plume within the FOV at high x/R. At the lowest position ($y/R < 0.05$), more than 90% percent of the images provide a sufficient thermal pattern close to the CTA sensors. With increasing y/R, the percentage quickly decreases to values below 20% at a height of $y/R = 0.14$. Nevertheless, the curve shows a sufficient amount of reliable data suitable for a comparison with the CTA sensors.

Figure 16 shows the comparison of the outwash velocity measured using the BOS velocimetry approach in gray and black, the reference data from the fiber-film CTA sensor array in red and the velocity profile of an outwash model from Preston (1994) as dashed black line. The raw BOS velocimetry data based on all data points with no masking are shown in gray and the data filtered based on the masking discussed in Fig. 9 is shown in black. The data measured with the BOS velocimetry approach show good quantitative agreement with the CTA data for heights of $y/R < 0.2$. Below this height, the shape of the outwash profile is captured well and the velocity magnitude is in a satisfactory range. Above $y/R = 0.2$ the BOS velocimetry data deviate from the CTA velocity profile. This trend is even stronger for the unfiltered data, which emphasizes the importance of a masking of unreliable areas in the BOS displacement fields.

The outwash model of Preston is a simple model based on the hover induced velocity out of ground effect, a correction function for hover IGE and the rotor radius. A deviation in the maximum outwash velocity between the model and the experimental data is apparent in Fig. 16. This may be related to a limited accuracy of the model or environmental influences, such as the ambient wind conditions. The general shape and magnitude predicted by the model are matched by the experiments over a wide range of heights above ground.

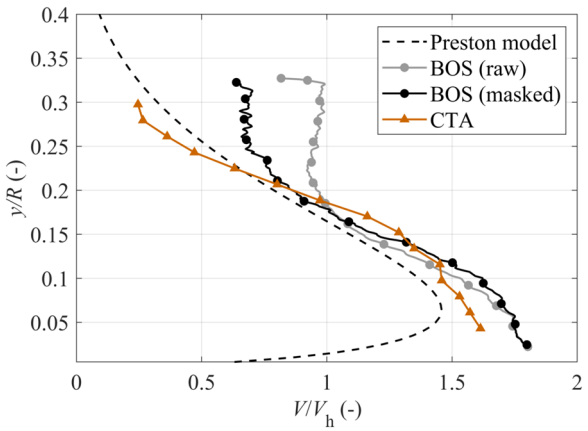

Fig. 16 Comparison of outwash velocity measured using BOS velocimetry, CTA fiber-film sensor array, and the Preston outwash model

In a further step, the time-resolved velocity data from the BOS velocimetry method can be compared to the CTA data. This comparison is given in Fig. 17a) for the highest CTA sensor position at $y/R = 0.30$ and in Fig. 17b) for the lowest CTA sensor position at $y/R = 0.04$. As expected from the data shown in Fig. 16, the mean velocity at $y/R = 0.04$ agrees well, whereas the mean velocity at $y/R = 0.30$ is overpredicted by the BOS velocimetry.

The BOS data were captured at a frequency of 420Hz and the CTA array was recorded at 50kHz. Furthermore, the application of the sum of correlation-method during the second correlation of the BOS data leads to a Gaussian weighted temporal average over 51 images. To account for these differences in the sampling frequency and to ease the comparison, a sliding average filter was applied to the CTA data.

The velocity fluctuations captured by both measurement techniques show comparable amplitudes. The time-resolved signals, on the other hand, do not show a good correlation. A possible reason is the distance between the CTA array and the evaluated plume resulting from either the constant offset in radial direction (x-direction) or a random offset in z-direction (location between camera and background).

5 Conclusions and outlook

The BOS displacement pattern caused by density gradients from hot engine exhaust gas was successfully used to quantitatively derive a velocity field in the outwash of helicopters hovering IGE. The technique was applied to outwash measurements of a CH-53G and a Bo105 helicopter.

The main take-aways are:

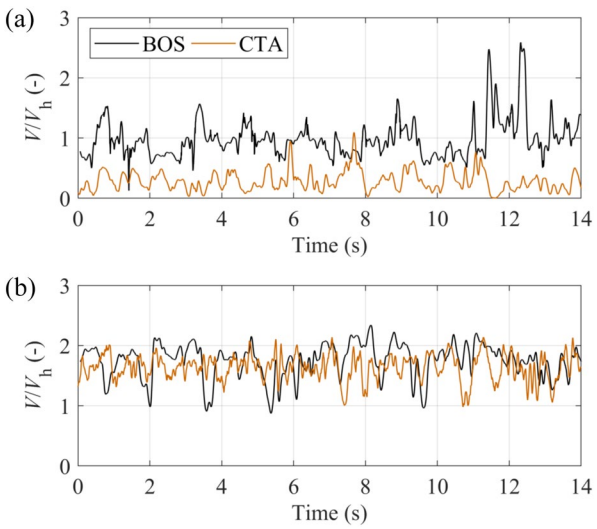

Fig. 17 Time-resolved velocity data from BOS velocimetry and CTA sensors at heights of **a** $y/R = 0.30$ and **b** $y/R = 0.04$

- BOS velocity can be used to qualitatively visualize the instationary flow topology.
- Based on data of both test cases the technique enables the calculation of well resolved quantitative velocity fields.
- The position of the exhaust plume has a major influence on the measurement reliability: The plume has to cover the area of interest to enable an evaluation and the plume location between camera and background has a strong influence on the accuracy of the calibration.
- The measured mean velocity in the rotor outwash compares well with the reference CTA measurements in areas of reliable thermal structures.

Acknowledgements This study was conducted within the framework of the DLR projects "URBAN–Rescue" and "ROME". The authors would like to thank Alexander Heintz, Stefan Koch, Anna Kostek, Markus Krebs, Felix Lößle, Markus Raffel, Florian Renneke, Clemens Schwarz, and the "Flight Experiments"–teams of DLR Braunschweig and WTD61 for their help during the experiments.

Author Contribution A.D.G. designed the experimental setup. All authors contributed equally to conducting the experiments related to this work. The BOS data processing was performed by J.N.B., whereas the CTA data was provided by C.C.W. J.N.B. wrote the main paper. All authors discussed the results and implications, and commented on the manuscript at all stages.

Funding Open Access funding enabled and organized by Projekt DEAL.

Data Availability No datasets were generated or analysed during the current study.

Declarations

Conflict of interests The authors declare no competing interests.

References

Biswas S, Qiao LA (2017) A comprehensive statistical investigation of schlieren image velocimetry (siv) using high-velocity helium jet. Exp Fluids 58(18):1–20. https://doi.org/10.1007/s00348-017-2305-2

Braukmann JN, Schwarz C, Wolf C, et al. (2023) Bos and hot-film analysis of a ch-53g helicopter wake in ground effect. In: American Helicopter Society 79th Annual Forum, 10.4050/F-0079-2023-18181

Brown R (2023) Understanding the downwash/outwash characteristics of evtol aircraft. In: CAA CAP 2576A, Civil Aviation Authority (CAA)

Bruun HH (1995) Hot-Wire Anemometry: Principles and Signal Analysis. Oxford University Press, Oxford, Great Britain

Hargather MJ, Lawson MJ, Settles GS et al. (2011) Seedless velocimetry measurements by schlieren image velocimetry. AIAA J 49(3):611–620. https://doi.org/10.2514/1.J050753

Jonassen DR, Settles GS, Tronosky MD (2006) Schlieren ?piv? for turbulent flows. Optics and Lasers in Engineering 44(3):190–207. https://doi.org/10.1016/j.optlaseng.2005.04.004, optical Methods in Heat Transfer and Fluid Flow

Meinhart CD, Wereley ST, Santiago JG (2000) A PIV algorithm for estimating time-averaged velocity fields. J Fluids Eng 122(2):285–289. https://doi.org/10.1115/1.483256

Mittelstaedt E, Davaille A, van Keken PE et al. (2010) A noninvasive method for measuring the velocity of diffuse hydrothermal flow by tracking moving refractive index anomalies. Geochem, Geophys, Geosyst 11(10):1–10. https://doi.org/10.1029/2010GC003227

Preston JR (1994) Vtol downwash / outwash operational effects model. In: AHS 50th annual forum

Raffel M (2015) Background-oriented schlieren (BOS) techniques. Exp Fluids 56(3):1–17. https://doi.org/10.1007/s00348-015-1927-5

Saijo T, Ganesh B, Huang A, et al. (2003) Development of unsteadiness in a rotor wake in ground effect. In: 21st AIAA Applied Aerodynamics Conference. American Institute of Aeronautics and Astronautics, https://doi.org/10.2514/6.2003-3519

Settles GS, Liberzon A (2022) Schlieren and bos velocimetry of a round turbulent helium jet in air. Opt Lasers in Eng 156:1–12. https://doi.org/10.1016/j.optlaseng.2022.107104

Silva MJ, Riser R (2011) Ch–47d tandem rotor outwash survey. In: American Helicopter Society 67th Annual Forum

Sugiura M, Tanabe Y, Sugawara H et al. (2017) Numerical simulations and measurements of the helicopter wake in ground effect. J Aircraft 54(1):209–219. https://doi.org/10.2514/1.c033665

Tanner PE, Overmeyer AD, Jenkins LN, et al. (2015) Experimental investigation of rotorcraft outwash in ground effect. In: American Helicopter Society 71st Annual Forum

Wolf CC, Weiss A, Schwarz C et al. (2022) Wake unsteadiness and tip vortex system of full-scale helicopters in ground effect. J Am Helicopter Soc 67(1):1–17. https://doi.org/10.4050/jahs.67.012010